Effects of Water Injection Strategies on Oxy-Fuel Combustion Characteristics of a Dual-Injection Spark Ignition Engine

Xiang Li [1,*](ID), Yiqiang Pei [2], Dayou Li [1], Tahmina Ajmal [1](ID), Khaqan-Jim Rana [1], Abdel Aitouche [3,4], Raouf Mobasheri [3,4] and Zhijun Peng [5,*]

1   School of Computer Science and Technology, University of Bedfordshire, Luton LU1 3JU, UK; dayou.li@beds.ac.uk (D.L.); tahmina.ajmal@beds.ac.uk (T.A.); khaqan.rana@beds.ac.uk (K.-J.R.)
2   State Key Laboratory of Engines, Tianjin University, Tianjin 300072, China; peiyq@tju.edu.cn
3   UMR 9189–CRIStAL—Centre de Recherche en Informatique Signal et Automatique de Lille, CNRS, Centrale Lille, Université de Lille, F-59000 Lille, France; abdel.aitouche@junia.com (A.A.); raouf.mobasheri@junia.com (R.M.)
4   Junia, Smart Systems and Energies, Université de Lille, F-59000 Lille, France
5   School of Engineering, University of Lincoln, Lincoln LN6 7TS, UK
*   Correspondence: xiang.li@beds.ac.uk (X.L.); jpeng@lincoln.ac.uk (Z.P.)

Abstract: Currently, global warming has been a serious issue, which is closely related to anthropogenic emission of Greenhouse Gas (GHG) in the atmosphere, particularly Carbon Dioxide (CO_2). To help achieve carbon neutrality by decreasing CO_2 emissions, Oxy-Fuel Combustion (OFC) technology is becoming a hot topic in recent years. However, few findings have been reported about the implementation of OFC in dual-injection Spark Ignition (SI) engines. This work numerically explores the effects of Water Injection (WI) strategies on OFC characteristics in a practical dual-injection engine, including GDI (only using GDI), P_{50}-G_{50} (50% PFI and 50% GDI) and PFI (only using PFI). The findings will help build a conceptual and theoretical foundation for the implementation of OFC technology in dual-injection SI engines, as well as exploring a solution to increase engine efficiency. The results show that compared to Conventional Air Combustion (CAC), there is a significant increase in BSFC under OFC. Ignition delay (θ_F) is significantly prolonged, and the spark timing is obviously advanced. Combustion duration (θ_C) of PFI is a bit shorter than that of GDI and P_{50}-G_{50}. There is a small benefit to BSFC under a low water-fuel mass ratio (R_{wf}). However, with the further increase of R_{wf} from 0.2 to 0.9, there is an increment of 4.29%, 3.6% and 3.77% in BSFC for GDI, P_{50}-G_{50} and PFI, respectively. As WI timing (t_{WI}) postpones to around $-30\ ^\circ$CA under the conditions of $R_{wf} \geq 0.8$, BSFC has a sharp decrease of more than 6 g/kWh, and this decline is more evident under GDI injection strategy. The variation of maximum cylinder pressure (P_{max}) and combustion phasing is less affected by WI temperature (T_{WI}) compared to the effects of R_{wf} or t_{WI}. BSFC just has a small decline with the increase of T_{WI} from 298 K to 368 K regardless of the injection strategy. Consequently, appropriate WI strategies are beneficial to OFC combustion in a dual-injection SI engine, but the benefit in fuel economy is limited.

Keywords: oxy-fuel combustion (OFC); water injection (WI) strategies; dual-injection spark ignition (SI) engine; simulation

1. Introduction

The global warming crisis has apparently been a severe problem over the last few decades. Furthermore, the 10 warmest years on record have occurred since 1998, with the 4 warmest years occurring since 2014 [1]. Hence, carbon neutrality has become a desperate need to resolve the climate crisis, as it is closely linked to anthropogenic Greenhouse Gas (GHG) emissions, particularly Carbon Dioxide (CO_2) [2–4]. To help achieve carbon neutrality by decreasing CO_2 emissions, a variety of new technologies have been developed

for passenger vehicles, such as hybrid electric, plug-in hybrid electric, lithium-ion battery electric, solar-powered, fuel-cell electric, etc. [5–7].

However, due to the relatively high cost and low torque output, these technologies are rarely utilised in non-road mobile machineries, such as vessels and boats. In order to realise zero CO_2 emissions in conventional Internal Combustion Engine (ICE) fuelled with fossil fuels, Oxy-Fuel Combustion (OFC) technology with Carbon Capture and Storage (CCS) has been an attractive alternative in recent decades. Yaverbaum initially proposed OFC technology, which was afterward widely applied in power stations [8–12]. Equation (1) and Table 1 present the OFC reaction process and the gas physicochemical properties, respectively. The discrepancies of physicochemical properties between CO_2 and nitrogen have significant impacts on OFC and Conventional Air Combustion (CAC). The chemical reaction indicates that OFC can take advantage of eliminating nitrogen during the combustion process. The comparison of gas properties shows that CO_2 heat capacity is much higher than nitrogen on a mole basis. Besides, both the thermal diffusivity and oxygen diffusion of CO_2 are much lower than those of nitrogen.

$$C_xH_y + \left(x + \frac{y}{4}\right)O_2 \rightarrow xCO_2 + \frac{y}{2}H_2O \qquad (1)$$
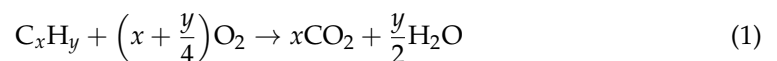
Table 1. Physicochemical properties of CO_2 and nitrogen at 1000 k and 0.1 MPa [13,14].

Property	CO_2	Nitrogen	Ratio (CO_2/Nitrogen)
Molecular weight	44	28	1.57
Density (kg/m^3)	0.5362	0.3413	1.57
Kinematic viscosity (m^2/s)	7.69×10^{-5}	1.2×10^{-4}	0.631
Specific heat capacity (kJ/kg K)	1.2343	1.1674	1.06
Thermal conductivity (W/m K)	7.057×10^{-2}	6.599×10^{-2}	1.07
Thermal diffusivity (m^2/s)	1.1×10^{-4}	1.7×10^{-4}	0.644
Mass diffusivity of O_2 (m^2/s)	9.8×10^{-5}	1.3×10^{-4}	0.778
Prandtl number	0.7455	0.7022	1.06
Emissivity and absorptivity	>0	~0	-

Regarding the study of OFC technology in Spark Ignition (SI) engines, Bilger [15] initially proposed a new approach named Internal Combustion Rankine Cycle (ICRC) in 1999. In recent years, Wu et al. [16–25] made a significant contribution to ICRC implementation in Port Fuel Injection (PFI) SI engines fuelled with propane under 40% to 70% oxygen volume fraction. Water Injection (WI) has been a proven method to control oxy-fuel combustion process of ICRC engines based on some findings [17–21]. Engine performance could be directly affected by the timing, duration, pressure, mass and temperature of WI. Thermal efficiency and indicated work could be enhanced by an appropriate rate of EGR matches with ignition timing and increased WI temperature. Li et al. [26] initially investigated the impacts of intake charge on OFC in a dual-injection SI engine fuelled with gasoline under GDI, P-G and PFI three injection strategies.

Based on this literature survey about OFC implementation in SI engines, most of them focused on PFI engines fuelled propane. However, few studies have been reported about the implementation of OFC in GDI engines or dual-injection SI engines. However, Gasoline Direct Injection (GDI) technology has become the mainstream of SI engines in academia and industry [27–35]. In 2005, an advanced technology named dual-injection was commercially applied to SI engines by Toyota [36]. Furthermore, with the advantages of flexible fuel injection, dual-injection SI engines have been a hot topic for researchers in recent years [37–42]. The thermal efficiency, gaseous and particulate emissions have been investigated in this type of engine by using gasoline plus various fuels such as methanol, ethanol and 2,5-dimethylfuran.

Therefore, the investigation of the effects of WI strategies on combustion characteristics of OFC in a dual-injection SI engine fuelled with gasoline was firstly reported in this article. It will provide valuable insight into the effects of WI strategies on OFC characteristics in a

practical dual-injection engine, including GDI (only using GDI), P_{50}-G_{50} (50% PFI and 50% GDI) and PFI (only using PFI). The findings will help build the conceptual and theoretical foundation for the OFC implementation in dual-injection SI engines, as well as exploring a solution to increase engine efficiency. This work belongs to the 'RIVER' project, which was proposed to develop a novel non-carbon boat with an environment-friendly powertrain system. The overview of the designed novel 'RIVER' system can be depicted in Figure 1, which mainly includes the subsystems of oxygen feeding, intake organisation, CO_2 capture and storage. Pure oxygen is mixed with recirculated gas (CO_2), then the mixture will enter into engine combustion chambers. Besides, the excess CO_2 can be captured in a storage tank to achieve zero carbon emissions.
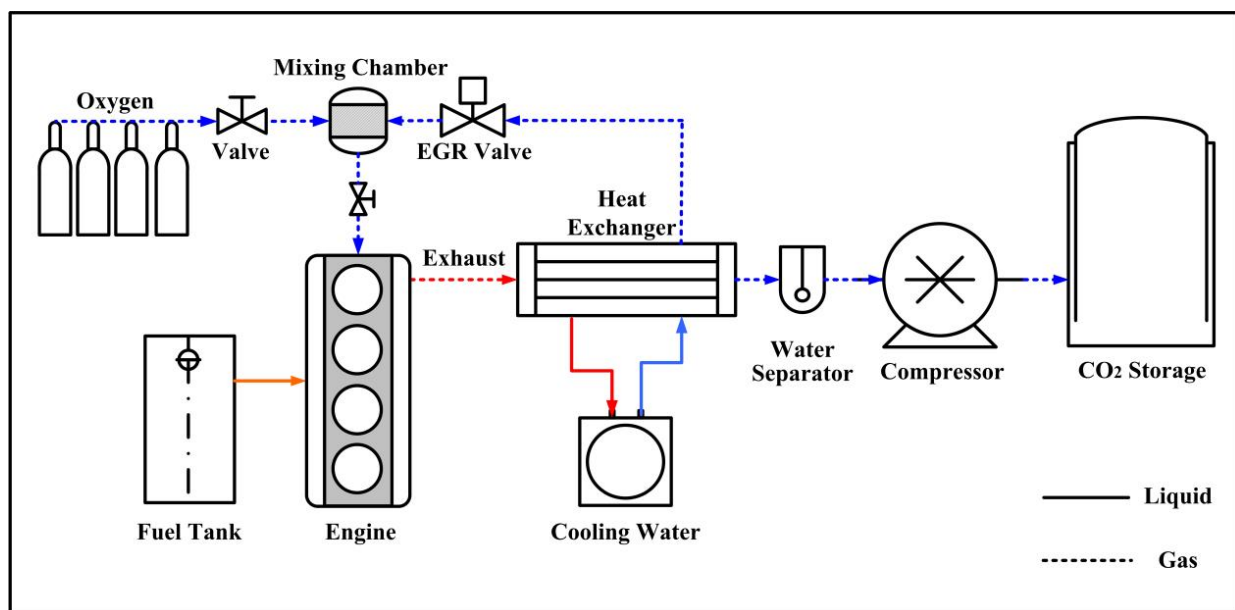
Figure 1. Schematic of OFC with CCS in the application of ICE.

2. Research Approach and Numerical Method

2.1. Research Approach and Key Parameters

In order to keep this numerical study well organised, the procedure can be summarised in Figure 2. First, the validation of this model is performed based on the experimental data of 2000 rpm-10 bar BMEP under CAC mode. Second, as nitrogen is replaced by CO_2, engine operation converts into the OFC mode with nitrogen replaced by CO_2, a comparison in performance between CAC and OFC is presented. Finally, the effects of WI mass, WI timing and WI temperature on OFC characteristics are explored and analysed in turn.

In order to increase the efficiency of water utilisation for optimising OFC process, it is usually injected directly into the engine chamber by a separated injector [17–21]. Figure 3 shows the schematic of two representatives.

The system presented in Figure 3a is adopted in this numerical study, which advantage is compact size, simple structure and control measure. A container coupled with a pump is utilised to deliver water to a rail. Afterward, water will be directly injected into combustion chambers with the assistance of an air booster. The booster provides a high WI pressure to enhance water droplets' breakup, diffusion and vaporisation.

The other strategy in Figure 3b does not include storage for water supply. Instead, the water vapour in the exhaust gas can be condensed and separated, then heated up prior to being recirculated and injected into the combustion chambers. The advantage of this system is that overall thermal efficiency can be improved by the benefit of water vaporisation inside the cylinder chamber and the waste heat recovery from the exhaust gas.
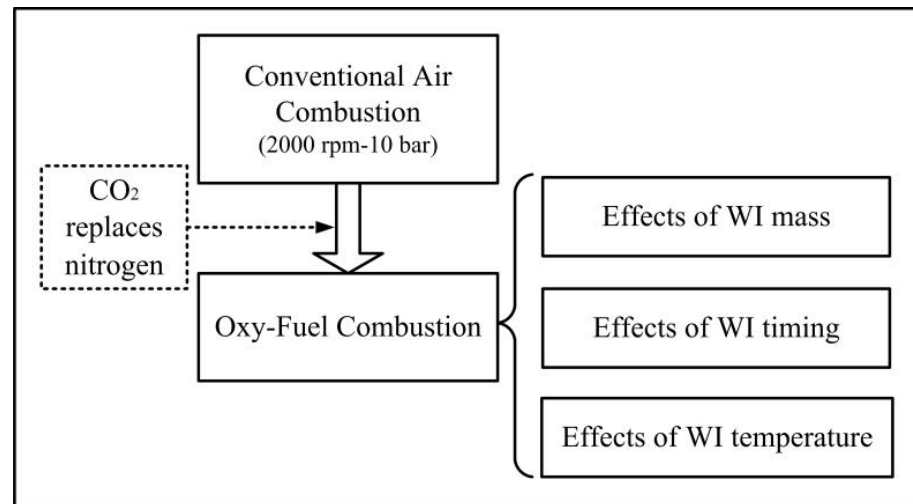
Figure 2. Flow chart of the research approach.
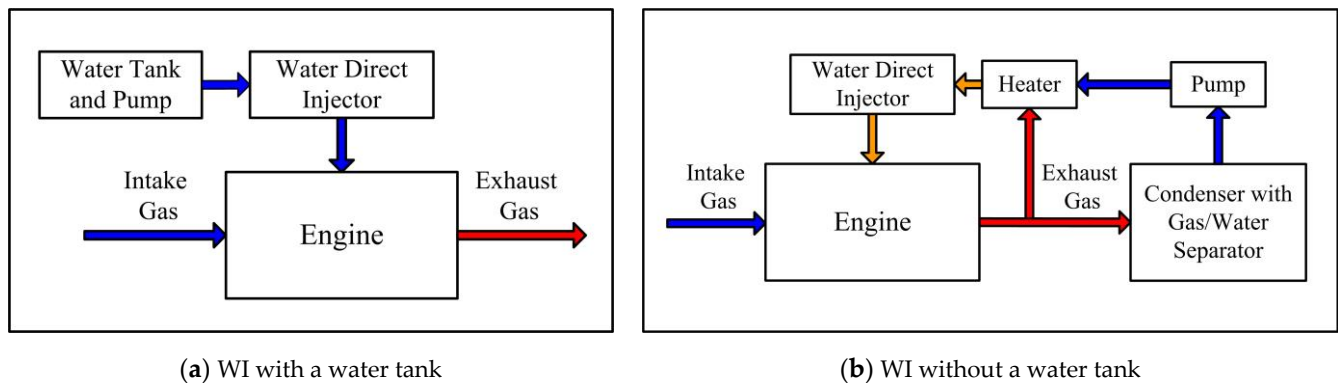
(**a**) WI with a water tank

(**b**) WI without a water tank

Figure 3. Schematic of typical WI systems in IC engines.

In order to make the parameters more visually, WI mass is parameterised by water-fuel mass ratio (R_{wf}) in Equation (2).

$$R_{wf} = \frac{\tau_w}{\tau_f} \tag{2}$$

Here, τ_w (mg/cycle) and τ_f (mg/cycle) denotes the injection quantity of water and fuel per engine cycle, respectively.

WI timing and WI temperature is abbreviated with t_{WI} and T_{WI}, respectively. Brake Specific Fuel Consumption (BSFC) is introduced to evaluate fuel consumption. φ_{CA10}, φ_{CA50} and φ_{CA90} represents the Crank Angle (CA) where 10%, 50% and 90% of the total heat has been released, respectively. Ignition delay (θ_F) represents the period between spark timing and φ_{CA10}. Combustion duration (θ_C) denotes the period between φ_{CA10} and φ_{CA90}.

During the study, engine operation is kept at a typical mid-high load of 2000 revolutions per minute (rpm) and 10 bar Brake Mean Effective Pressure (BMEP). The spark timings are fixed under the conditions of $R_{wf} = 0$. WI pressure is maintained at 60 bar to ensure the injected water is in the liquid state. The water boiling point at 60 bar is around 549 K, which is much higher than the WI temperature (298 K to 368 K) in this study. Besides, to make the investigation process more explicit, the throttle opening angle, fuel injection timings, intake temperature and Oxygen Mass Fraction (OMF) remain constant with CAC mode throughout this study.

2.2. Engine and Testbed

The model of numerical study is set up based on a practical turbocharged dual-injection SI engine fuelled with gasoline. The engine specifications and testbed overview are presented in Table 2 and Figure 4, respectively. The used fuel of this study is commercial gasoline, which physical and chemical parameters are shown in Table 3. Regarding the data collection and analysis of the test, cylinder pressure is measured and analysed by spark-plug type piezo-electric sensors (AVL-GH13Z), a crank sensor (Kistler 2614CK1), a charge amplifier (Kistler 5018A) and a combustion analyser (AVL 641). The pressure data are recorded and averaged by 200 consecutive cycles to ensure the accuracy of measurements. A direct current electrical dynamometer measures and controls the engine's speed and torque in real-time. A programmable Electronic Control Unit (ECU) is used to adjust the ignition, fuel injection and other engine operating parameters. The air-fuel ratio is kept constant at stoichiometric ratio (lambda = 1 ± 0.01). The uncertainties of the measured parameters in the test are shown in Table 4 by the root mean square method.

Table 2. Engine specifications.

Items	Content
Engine type	Four-cylinder; Four-stroke
Bore × Stroke (mm)	82.5 × 92
Displacement (L)	2.0
Injection type	Dual-injection (PFI plus GDI)
Intake type	Turbocharged
Compression ratio	9.6:1
Rated speed (rpm)	5500
Rated power (kW)	160
Maximum Torque (N·m)	320
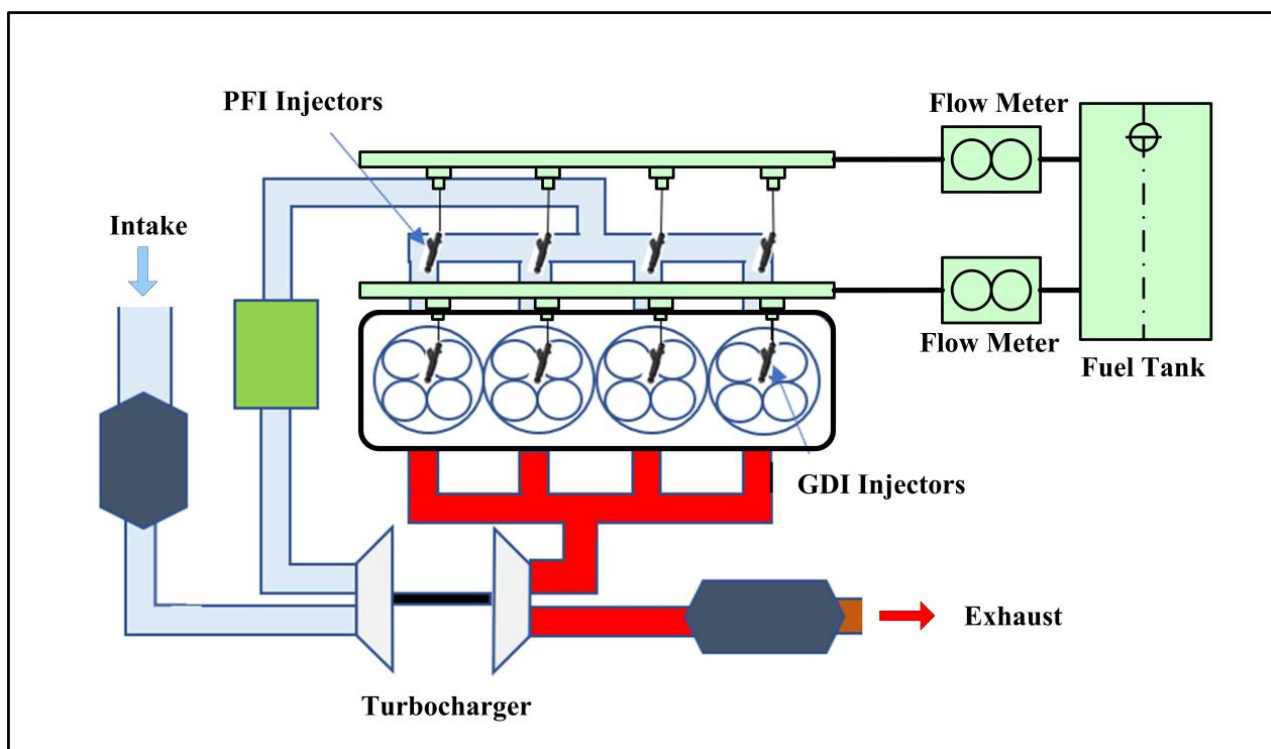
Figure 4. Schematic of engine testbed.

Table 3. Fuel properties.

Items	Content
Fuel type	Gasoline
Chemical formula	C5-C12
Relative molecular mass	95–120
Gravimetric carbon content (%)	86.4
Gravimetric hydrogen content (%)	13.6
Gravimetric oxygen content (%)	<0.1
Research octane number	95
Density (20 °C) (kg/L)	0.73
Dynamic viscosity (20 °C) (mPa·s)	0.52
Kinematic viscosity (20 °C) (mm^2/s)	0.71
Surface tension (20 °C) (N/m)	22
Boiling range (°C)	30–200
Low heating value (kJ/kg)	44,300
Latent heat of vaporisation (kJ/kg)	370
Laminar flame speed (20 °C) (m/s)	0.33
Stoichiometric air-fuel ratio	14.7

Table 4. Uncertainties of measured parameters.

Measured Parameters	Uncertainty (%)
Engine speed	±0.1
BMEP	±0.1
BSFC	±0.2
Pressure	±0.1
Crank angle	±0.1
Lambda	±0.3
Coolant temperature	±0.4
Intercooler output temperature	±0.4

2.3. Model Description

The model used in this study is set up based on GT-Power software, which is an industry-standard simulation software and widely used both industry and academia to predict combustion performance of SI engines [43–46].

In this model, the engine configuration settings are according to its detailed specifications, such as basic geometry of pipes, engine displacement, cylinder bore, connecting rod length, valves, etc. The heat transfer process in ICE can be classified into thermal conduction, thermal convection, thermal radiation and thermal vaporisation. The heat transfer submodel is set to be 'Woschni model', which was put forward to provide an instantaneous, spatially averaged heat transfer coefficient for the evaluation of heat transfer rate to the cylinder walls [47–49]. Some key correlations in the 'Woschni model' are given by Equations (3)–(5).

$$Q_W = \int_0^{cycle} \sum_i h A_i (T - T_{wi}) d\varphi \tag{3}$$

$$h = 110 d^{-0.2} P^{0.8} T^{-0.53} (C_1 c_m + w_c)^{0.8} \tag{4}$$

$$w_c = C_2 \frac{V_S T_1}{P_1 V_1} (P - P_0) \tag{5}$$

Here, Q_W is total heat transferred; h is heat transfer coefficient; A_i is heat absorbing area of the surfaces; T is in-cylinder mean gas temperature; T_{wi} is mean surface temperature of A_i; φ is CA; d is cylinder bore diameter; P is cylinder pressure; T is in-cylinder mean gas temperature; C_1 is a constant related to airflow velocity coefficient; c_m is mean piston speed; w_c is gas velocity caused by combustion; C_2 is a constant related to combustion chamber;

V_S is cylinder volume; P_0 is cylinder pressure when the engine is started. T_1, P_1 and V_1 is cylinder temperature, pressure and volume at the beginning of compression, respectively.

The 'SI turbulent flame combustion model' is chosen and set up for the submodel of combustion and heat transfer. This submodel is commonly used to predict the in-cylinder burn rate, knocking occurrence and emissions for SI engines [43]. Moreover, the flame-wall interactions can be calculated in this submodel according to the settings of cylinder geometry, spark location, head region and piston cup. Some key formulas are presented as Equations (6)–(9).

$$S_L = S_{L,0}(\frac{T_u}{T_{ref}})^{\alpha}(\frac{p}{p_{ref}})^{\beta} = (B_m - B_O(O - O_m)^2)\left(\frac{T_u}{T_{ref}}\right)^{\alpha}\left(\frac{p}{p_{ref}}\right)^{\beta} f(D) \tag{6}$$

$$f(D) = 1.0 - 0.75\lambda_{DEM}(1.0 - (1.0 - 0.75\lambda_{DEM}D)^7) \tag{7}$$

$$\alpha = 2.4 - 0.271O^{3.51} \tag{8}$$

$$\beta = -0.357 + 0.14O^{2.77} \tag{9}$$

Here, S_L is laminar flame speed; $S_{L,0}$ is laminar flame speed under the condition of 298 K and 101.325 kPa; T_u is unburned gas temperature; T_{ref} is 298 K; α is temperature exponent; p is pressure; p_{ref} is 101.325 kPa; β is pressure exponent; B_m is maximum laminar speed; B_O is laminar speed roll-off value; O is in-cylinder equivalence ratio; O_m is equivalence ratio at maximum speed; $f(D)$ is dilution effect; D is mass fraction of the residuals in the unburned zone; λ_{DEM} is dilution effect multiplier.

2.4. Model Validation

Figures 5 and 6 show the model validation by comparing cylinder pressure and Heat Release Rate (HRR) between experimental and simulation results at 2000 rpm-10 bar under CAC mode with GDI, P_{50}-G_{50} and PFI three injection strategies. The time-step sensitivity has also been considered to assure the accuracy of the simulation results further. It can be observed that the cylinder pressure and HRR curves in experimental conditions have a good match with those of simulation. Furthermore, the magnitude and position for the peaks of curves are correctly predicted. Therefore, this model is eligible to make a reasonable prediction in this study.
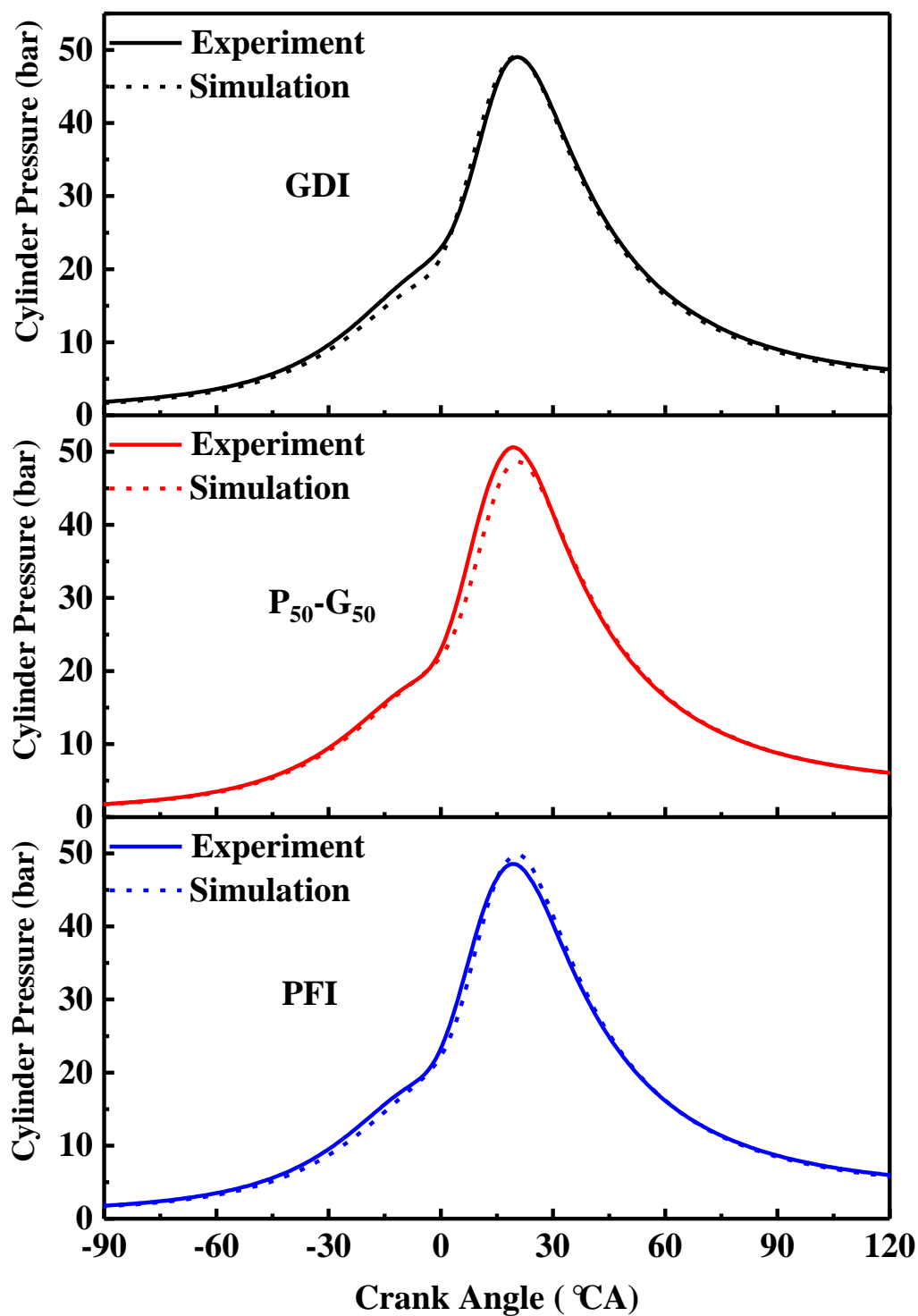
Figure 5. Comparison of cylinder pressure between experimental and simulation results at 2000 rpm-10 bar.
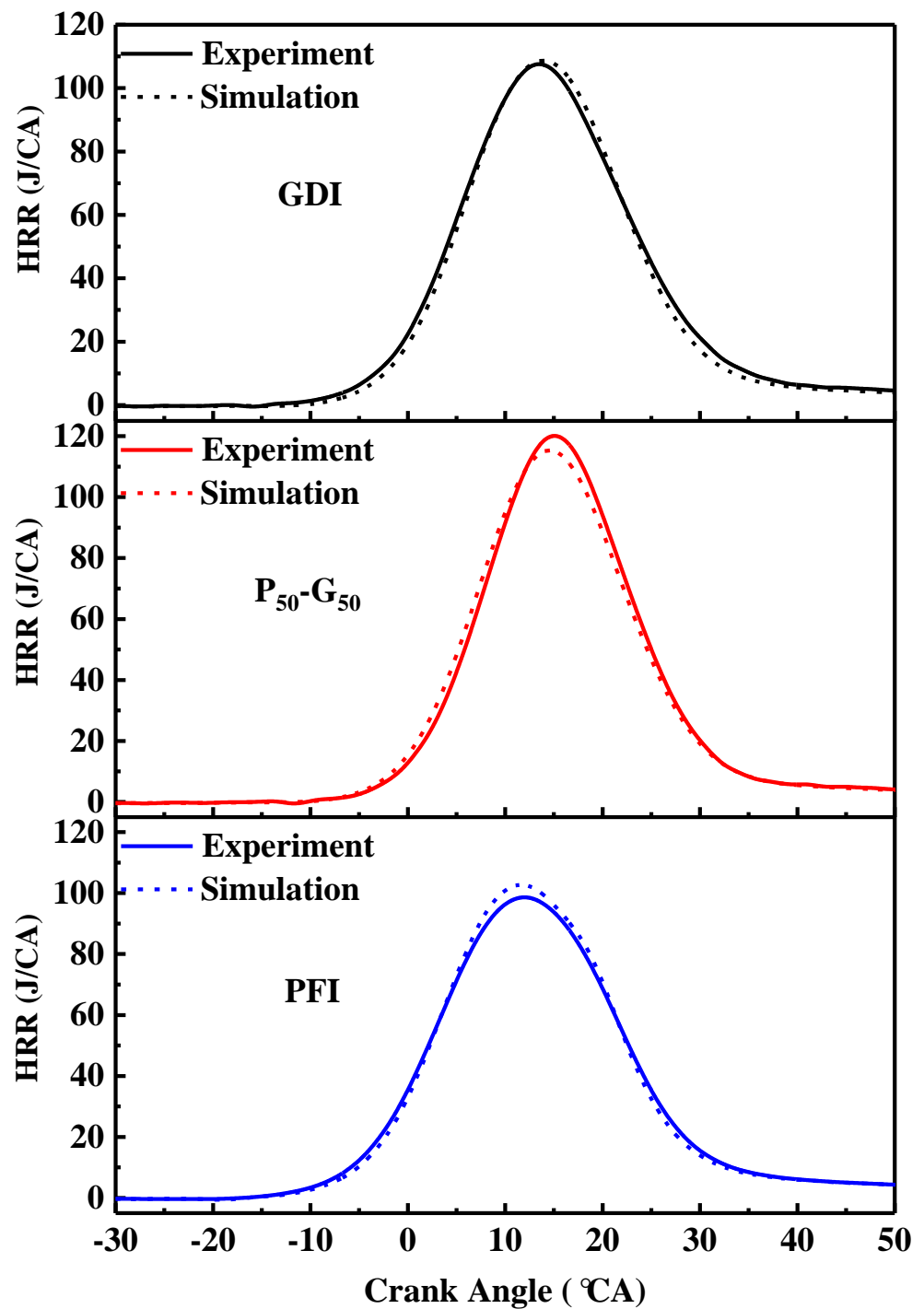
Figure 6. Comparison of HRR between experimental and simulation results at 2000 rpm-10 bar.

3. Results and Discussion

3.1. Comparison between CAC and OFC

Figure 7 presents the comparison of HRR between CAC and OFC under 2000 rpm-10 bar. The spark timing is optimised to be the minimum advance for Maximum Brake Torque (MBT) or Knock Limited Spark Advance (KLSA) for each condition.
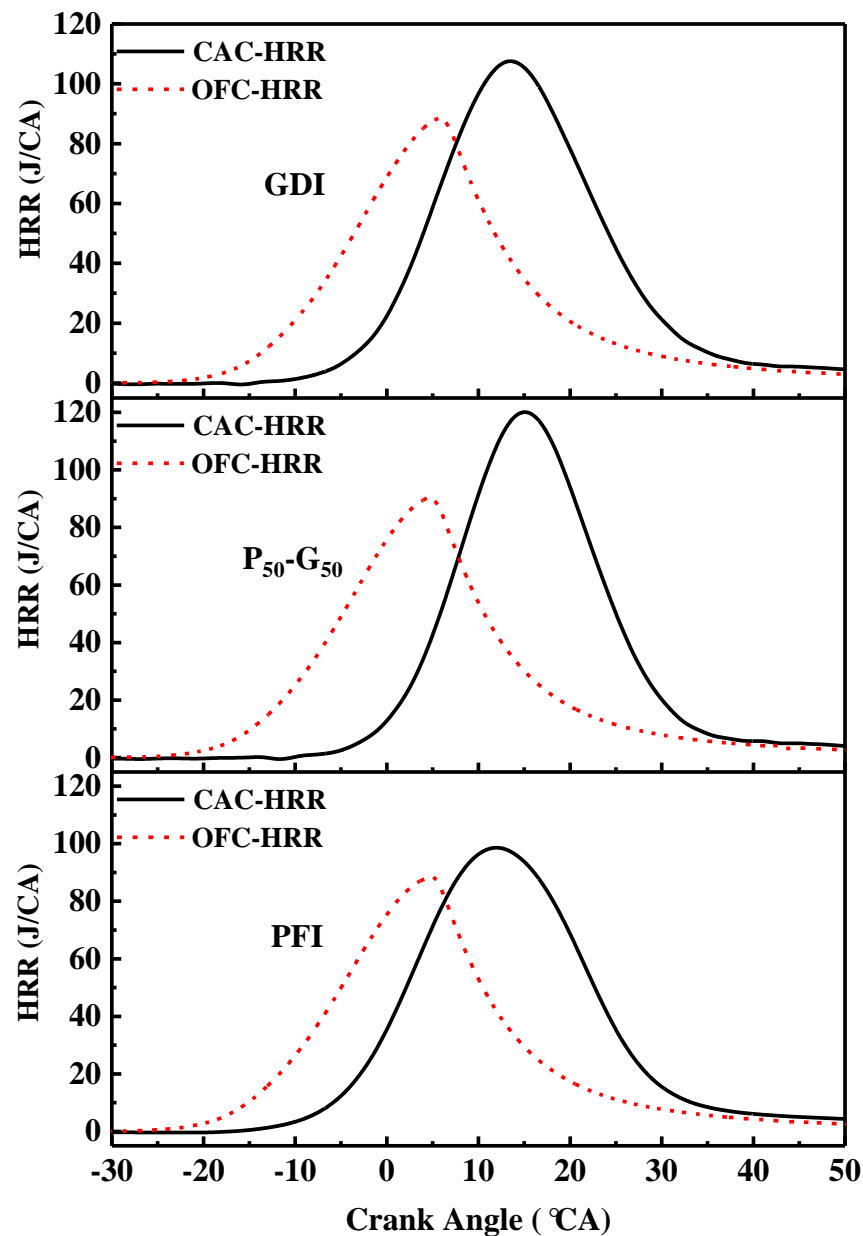
Figure 7. Comparison of HRR between CAC and OFC.

It can be seen that the peaks of HRR under OFC are generally about 8 degrees advanced than CAC. The peaks of HRR curves decrease from around 110 J/CA of CAC to 90 J/CA of OFC. This is mainly because the engine knocking would occur with the excessively advanced sparking timing at 2000 rpm-10 bar under CAC, and it can be easily avoided since the thermal diffusivity of CO_2 is much lower than that of nitrogen.

Figures 8 and 9 shows the comparison of BSFC, spark timing, θ_F and θ_C between CAC and OFC. It can be seen that BSFC is 317.269 g/kWh, 317.519 g/kWh and 317.524 g/kWh for GDI, P_{50}-G_{50} and PFI, respectively. There is a significant increase of around 68 g/kWh compared to that of the CAC mode. This is mainly because the thermal diffusivity of CO_2 is much lower than nitrogen, resulting in a great difference in flame transmission, which would increase the heat loss under OFC. Even though there are also offset effects caused by the higher thermal conductivity of CO_2 than that of nitrogen.

The behaviour can be further explained by the significantly advanced spark timing and prolonged θ_F under OFC compared to CAC. It is similar to some previous findings

of oxy-fuel burners, which conclude that the ignition delay of a mixture of O_2/CO_2 is significantly higher than that of an O_2/N_2 mixture with a similar oxygen fraction [50,51].
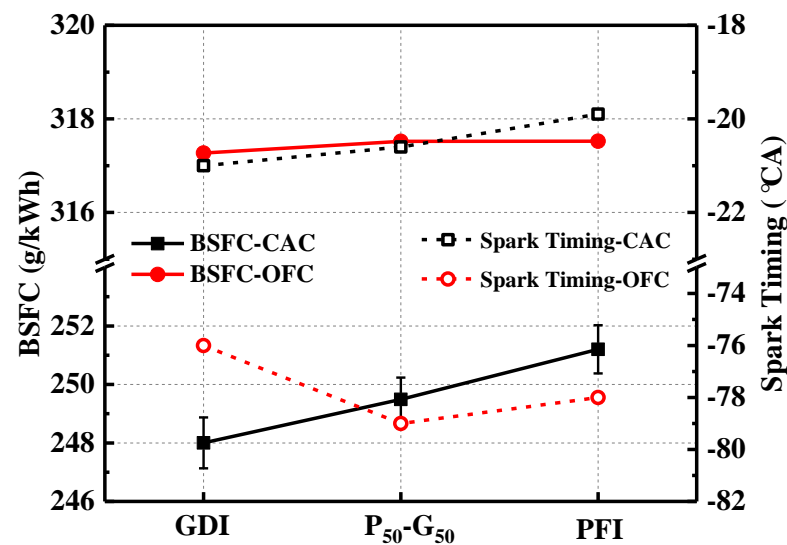
Figure 8. Comparison of BSFC and spark timing between CAC and OFC.
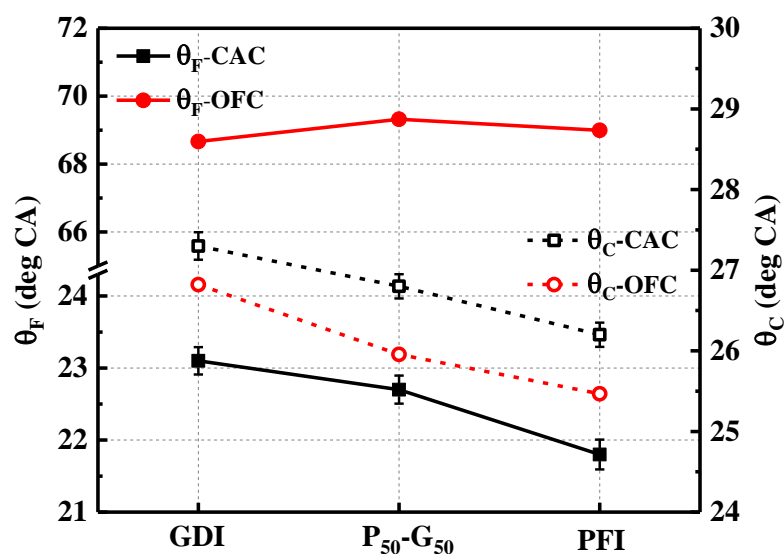
Figure 9. Comparison of θ_F and θ_C between CAC and OFC.

Besides, there is no significant difference in θ_C between OFC and CAC. In the meantime, the θ_C of PFI under OFC is 25.5 degrees, which is a bit shorter than 26.8 degrees of GDI and 26 degrees of P_{50}-G_{50}. This can be attributed to that compared to P_{50}-G_{50} and GDI, a more homogenous gas-fuel mixture under PFI strategy can help accelerate flame development.

3.2. Effects of WI Mass on OFC Performance

The effects of R_{wf} are discussed in this section, which includes the analysis of BSFC, maximum cylinder pressure (P_{max}), φ_{CA50}, HRR and in-cylinder temperature under three injection strategies (GDI, P_{50}-G_{50} and PFI). Meanwhile, in order to make the research objective clear and straightforward, t_{WI} and T_{WI} is fixed at $-60\,°$CA and 298 K, respectively.

As shown in Figure 10, BSFC is quite sensitive to R_{wf}. With the increase of R_{wf} from 0 to 0.2, there is a small decrease in BSFC regardless of the injection strategy. The lowest BSFC is each 316.647 g/kWh, 316.497 g/kWh and 316.358 g/kWh for GDI, P_{50}-G_{50} and

PFI, which has a slight saving rate of 0.196%, 0.322% and 0.367% than that of $R_{wf} = 0$, respectively. This can be attributed to the increased working medium and oxygen atom concentration from injected water.
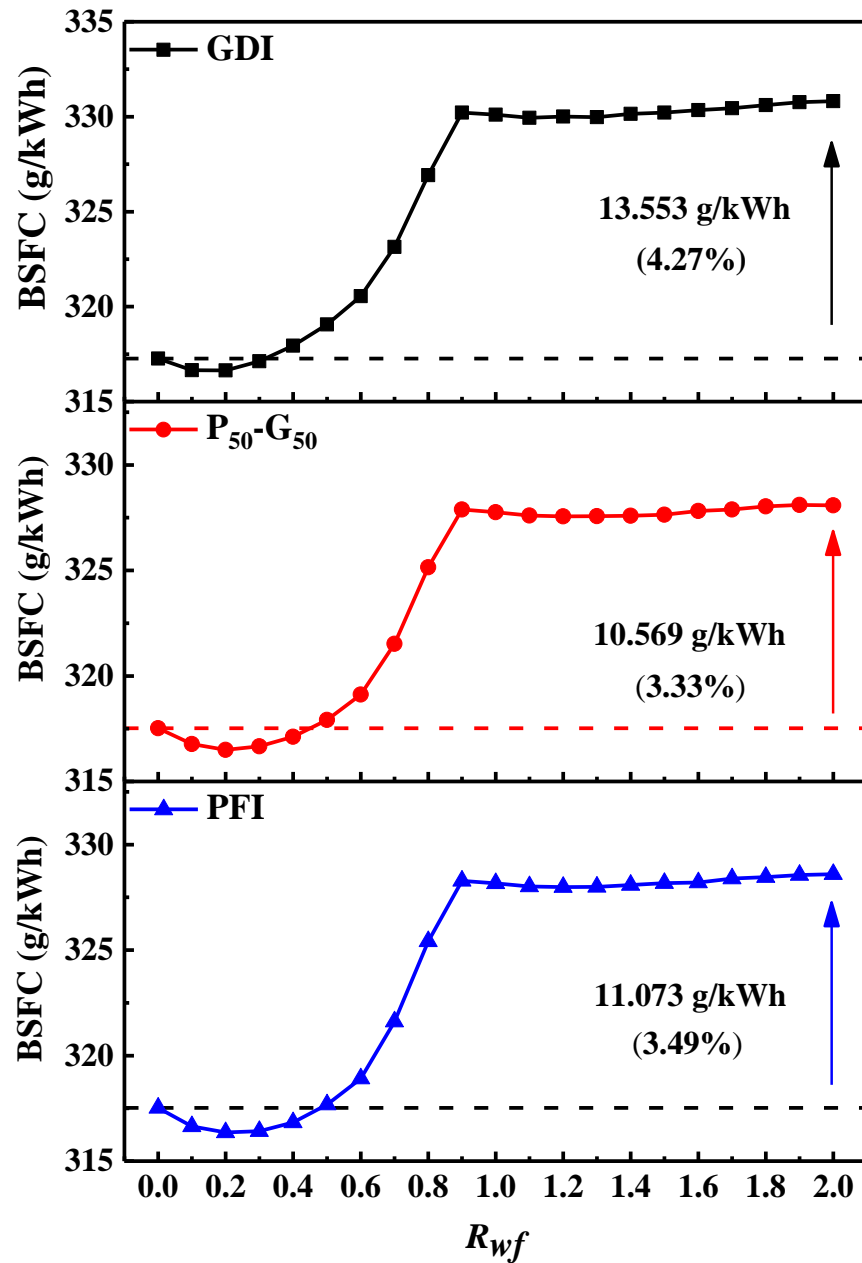
Figure 10. Effects of R_{wf} on BSFC.

However, an overall growth trend can be observed in BSFC with the further increase of R_{wf} from 0.2 to 0.9, which is an increment of 4.29%, 3.6% and 3.77% for GDI, P_{50}-G_{50} and PFI, respectively. Moreover, by further increasing R_{wf} from 0.9 to 2.0, the trend of BSFC would become quite stable. This indicates that an excessive amount of injected water will increase BSFC. However, the deterioration is not serious due to water's positive effect on combustion by the increased working medium and oxygen concentration.

The variations can be further explained in Figures 11 and 12, which show the effects of R_{wf} on combustion characteristics by P_{max}, φ_{CA50}, HRR and in-cylinder temperature. It demonstrates that the changing trends in combustion characteristics are similar for GDI, P_{50}-G_{50} and PFI. With the increase of R_{wf} from 0 to 0.6, P_{max} has a reduction of around 4.5

bar and φ_{CA50} is delayed by around 2.5 degrees. With further increased R_{wf}, both P_{max} and φ_{CA50} remain broadly stable with a minor fluctuation. In the meantime, HRR and in-cylinder temperature are also sensitive to R_{wf}. Under all the three injection strategies, as the R_{wf} increases from 0 to 1.0, the peak of HRR is postponed by around 1 degree whilst the peak of in-cylinder temperature reduces about 180 K. Afterwards, HRR and in-cylinder temperature will be less affected by further increasing R_{wf}.
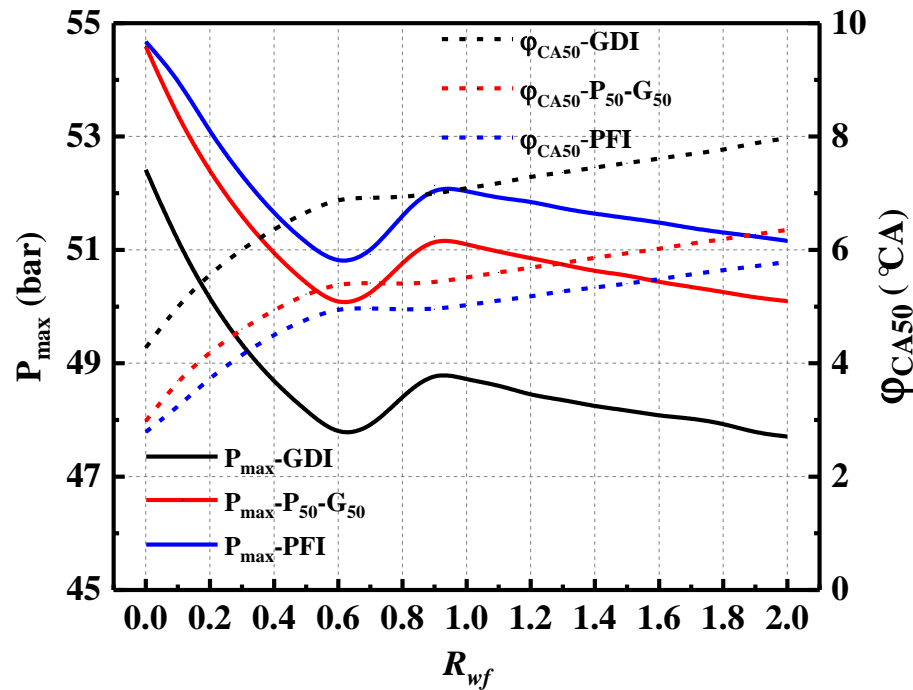
Figure 11. Effects of R_{wf} on P_{max} and φ_{CA50}.
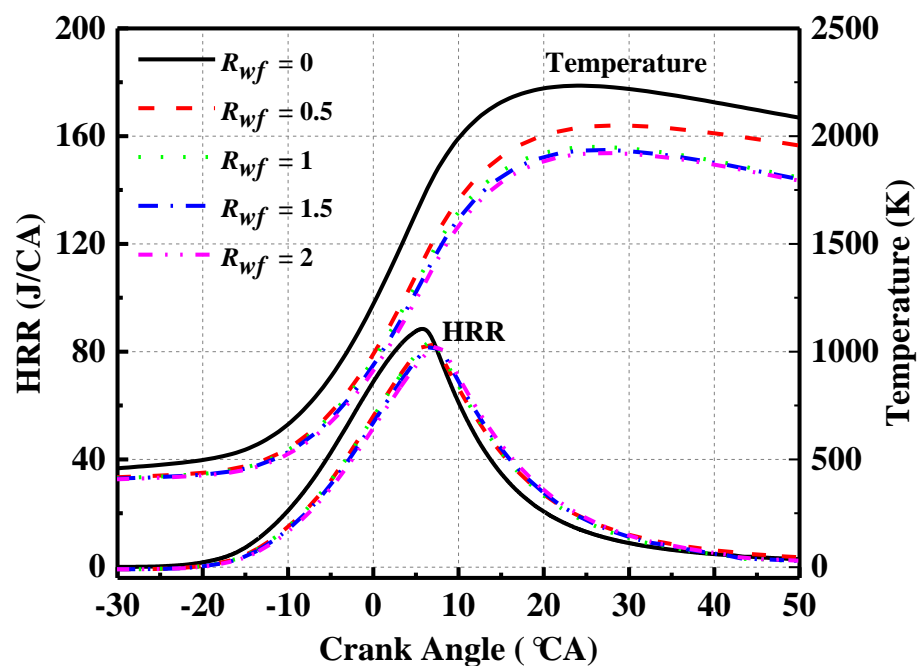
(**a**) GDI

Figure 12. *Cont.*
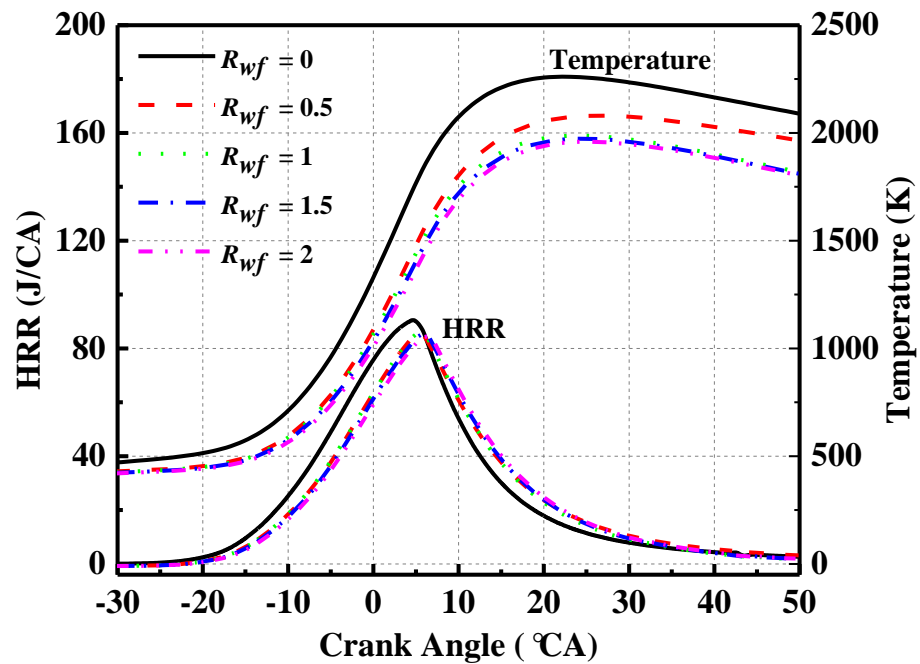
(**b**) P$_{50}$-G$_{50}$
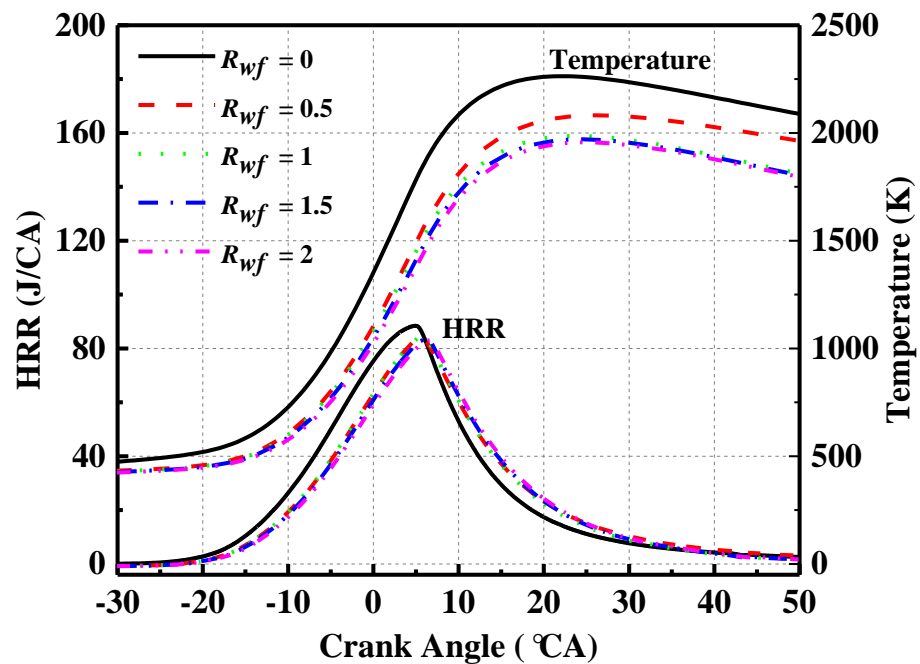
(**c**) PFI

Figure 12. Effects of R_{wf} on HRR and in-cylinder temperature.

3.3. Effects of WI Timing on OFC Performance

Figure 13 presents the effects of t_{WI} on BSFC under three injection strategies (GDI, P$_{50}$-G$_{50}$ and PFI). Meanwhile, T_{WI} is held constant at 298 K in this section.

On the whole, the relatively lower BSFC generally appear with low R_{wf}. The lowest BSFC appears on the operating condition of 't_{WI} = −70 °CA, R_{wf} = 0.1', 't_{WI} = −70 °CA, R_{wf} = 0.2' and 't_{WI} = −70 °CA, R_{wf} = 0.2' for GDI, P$_{50}$-G$_{50}$ and PFI, respectively. The

corresponding values are each 316.638 g/kWh, 316.383 g/kWh and 316.172 g/kWh, which provides a limited benefit of 0.199%, 0.358% and 0.426% than that of R_{wf} = 0, respectively.

Besides, it can be observed that BSFC is less affected by t_{WI} under the conditions of low R_{wf}. On the conditions of $R_{wf} \leq 0.5$, the fluctuation of BSFC is generally kept in a narrow range with the delay of t_{WI} from −100 °CA to −30 °CA under all three injection strategies.

Under the conditions of high R_{wf} ($R_{wf} \geq 0.8$), BSFC is strongly affected by t_{WI}. As t_{WI} postpones from −100 °CA to −30 °CA, BSFC has a sharp decrease of more than 6 g/kWh. Furthermore, this trend becomes more obvious under GDI injection strategy. Because the negative effects on the gas-fuel mixture from the vaporisation process of injected water are a bit stronger under GDI. The variation of BSFC can be attributed to the combustion characteristics, which are presented with P_{max}, φ_{CA50}, HRR and in-cylinder temperature in Figures 14 and 15.

As shown in Figure 14, P_{max} shows a monotonic increase with the delay of t_{WI} from −100 °CA to −30 °CA. The decreased tendency is more apparent under the conditions of R_{wf} = 1.0, particularly with GDI strategy. In the meantime, φ_{CA50} generally shows a decreasing trend to around 5 °CA at t_{WI} = −30 °CA, which is also helpful to improve fuel efficiency. Figure 15 shows the effects of t_{WI} on HRR and in-cylinder temperature under GDI with R_{wf} = 1.0. With the postpone of t_{WI} from −100 °CA to −40 °CA, the peak of HRR is advanced by 4.5 °CA, and the peak of in-cylinder temperature is significantly increased by 247 K. With the delay of t_{WI}, the improvement in combustion performance is mainly because the cooling effect is getting weaker by reducing the period of water vaporisation.

(**a**) GDI
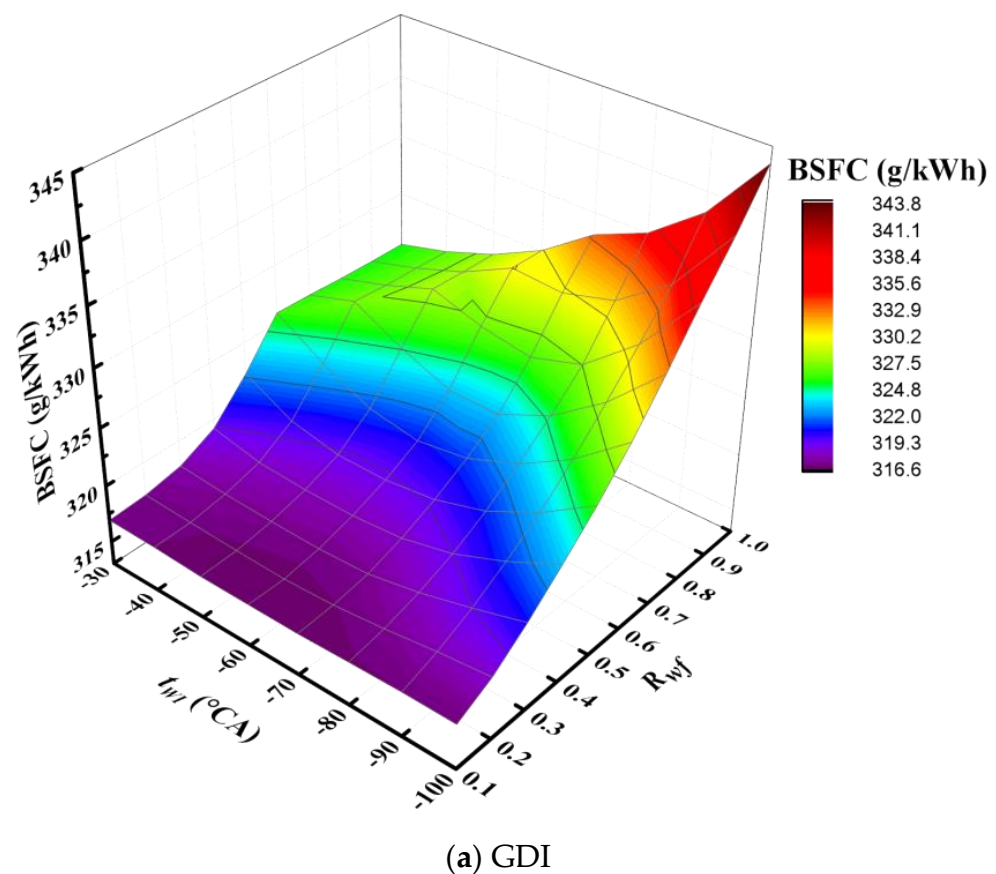
Figure 13. *Cont.*
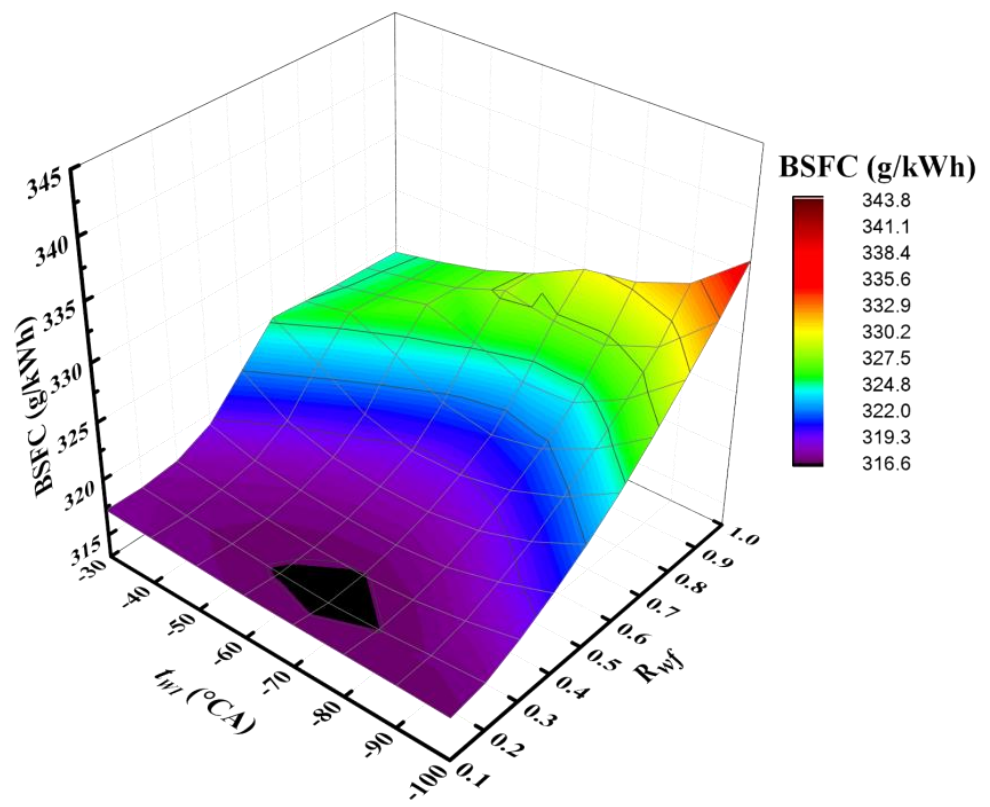
(**b**) P$_{50}$-G$_{50}$
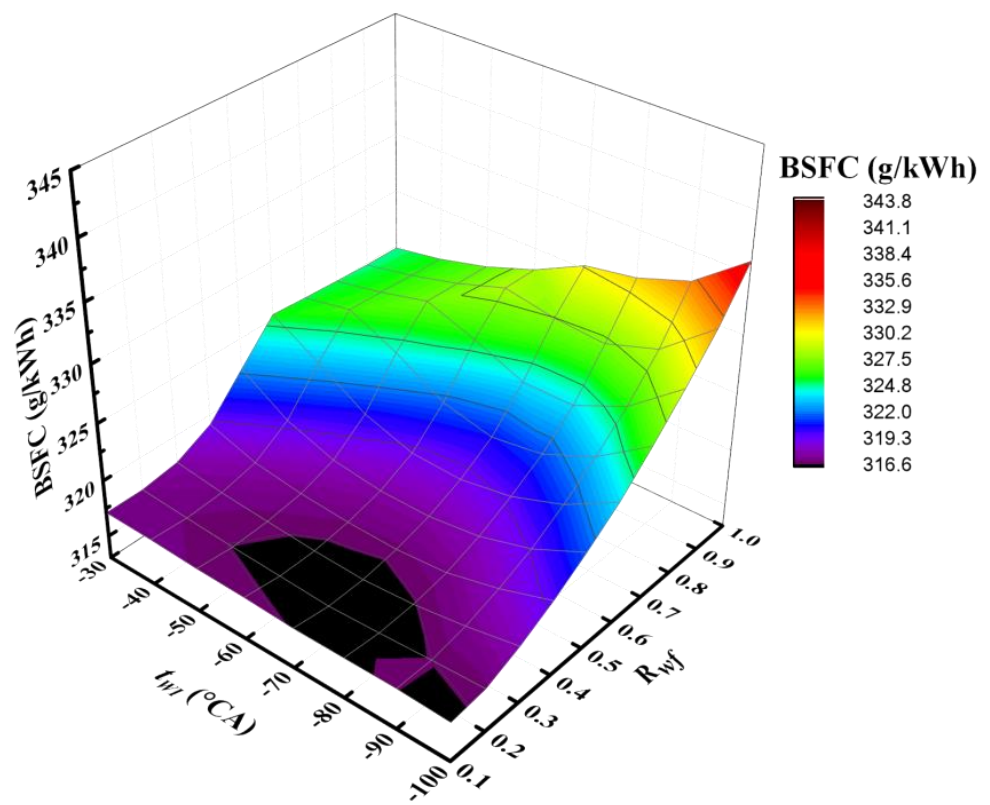
(**c**) PFI

Figure 13. Effects of t_{WI} on BSFC.
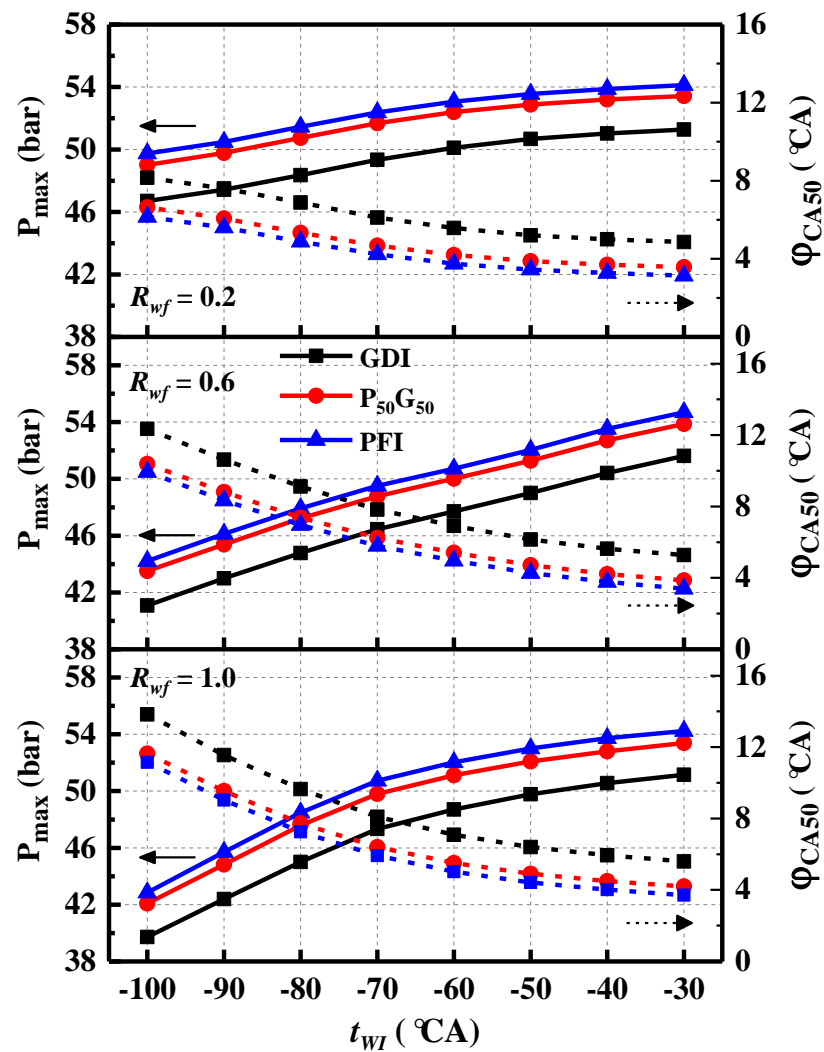
Figure 14. Effects of t_{WI} on P_{max} and φ_{CA50} (R_{wf} = 0.2, 0.6, 1.0).
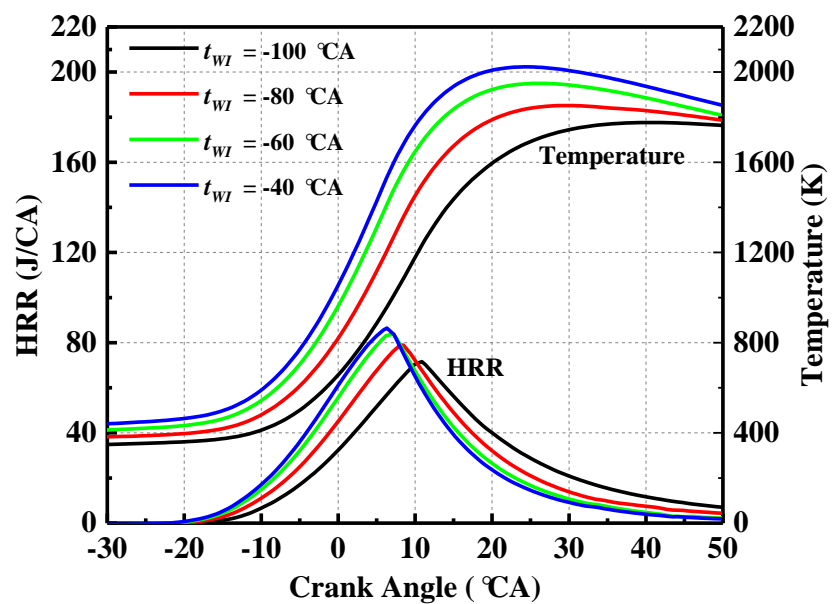
Figure 15. Effects of t_{WI} on HRR and in-cylinder temperature (GDI; R_{wf} = 1.0).

3.4. Effects of WI Temperature on OFC Performance

Figure 16 shows the effects of T_{WI} on BSFC under GDI, P_{50}-G_{50} and PFI injection strategies. In the meantime, t_{WI} is fixed at $-60\ ^\circ$CA in this section. It can be seen that BSFC is not sensitive to T_{WI}, it generally has a small decline with the increase of T_{WI} from 298 K to 368 K regardless of the injection strategy. The most significant decline is just around 3.5 g/kWh under R_{wf} = 1.0. Besides, the lowest BSFC are each 316.291 g/kWh, 316.068 g/kWh and 315.884 g/kWh, providing a limited saving rate of 0.308%, 0.457% and 0.516% than that of R_{wf} = 0, respectively.

Figure 17 presents the effects of T_{WI} on P_{max} and φ_{CA50} under R_{wf} = 0.2, 0.6 and 1.0. The variation of P_{max} and φ_{CA50} is less affected by T_{WI} compared to the effects of R_{wf} or t_{WI}. By increasing T_{WI} from 298 K to 368 K, P_{max} just presents an increase of around 0.5 bar, and whilst φ_{CA50} would be advanced by about 0.25 degrees. This is mainly because that by increasing T_{WI}, the suppression of combustion would become slightly weaker during the process of heat absorption by the cooling effect of water. Moreover, increasing T_{WI} would accelerate the vaporisation rate of water, leading to fewer negative effects on combustion [52].

This can also be explained by Figure 18, which is one example to show the effects of T_{WI} on HRR and in-cylinder temperature. It shows that by increasing T_{WI} from 308 K to 368 K, the peak of HRR and in-cylinder temperature have a slight increase of 0.47 J/CA and 19.5 K, respectively.

(**a**) GDI
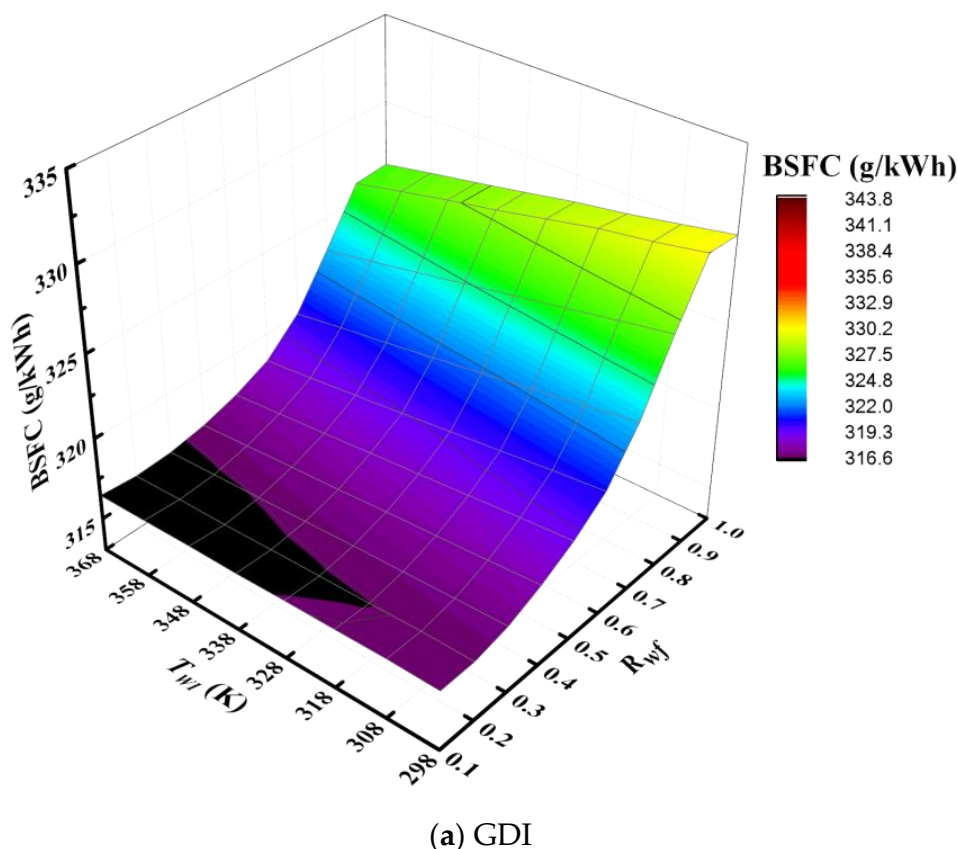
Figure 16. *Cont.*
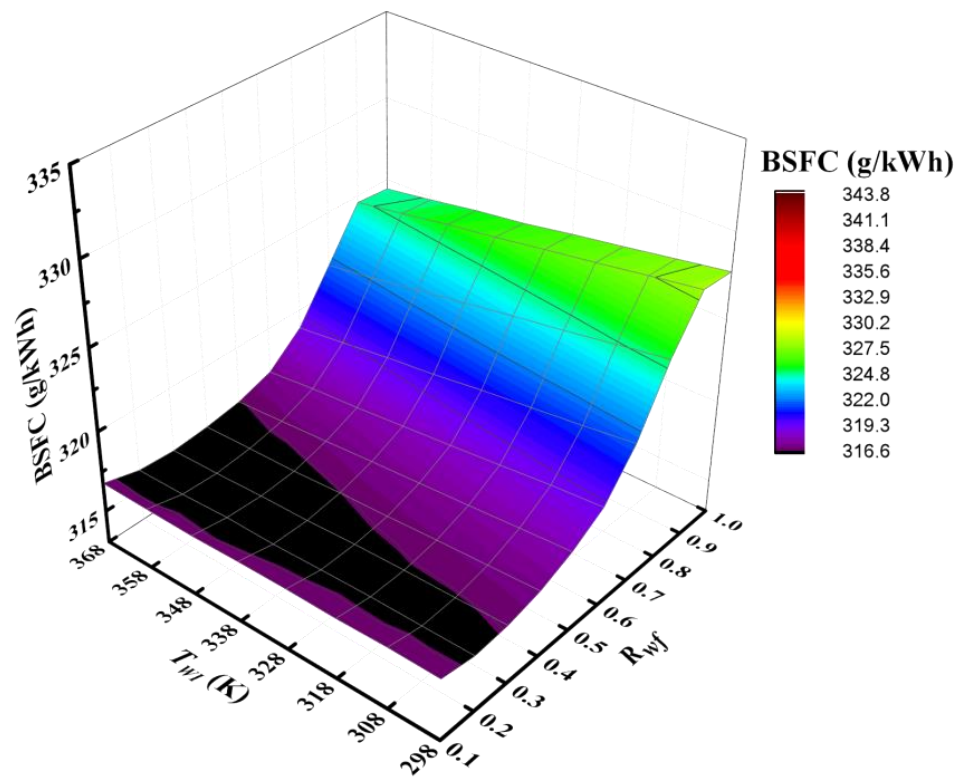
(**b**) P$_{50}$-G$_{50}$
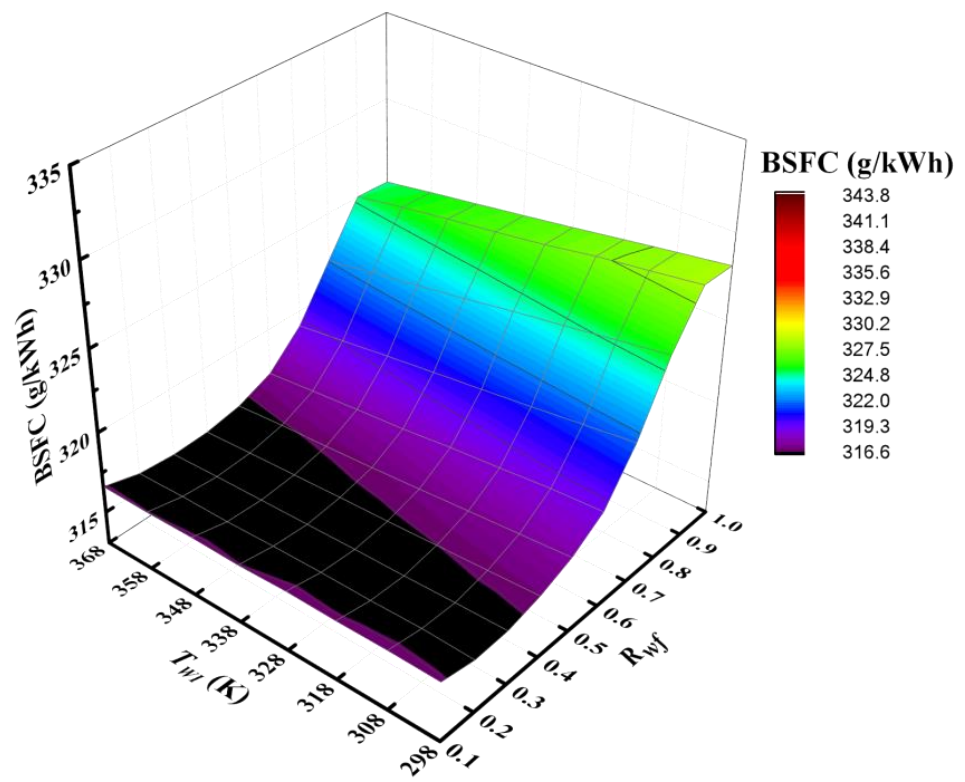
(**c**) PFI

Figure 16. Effects of T_{WI} on BSFC.
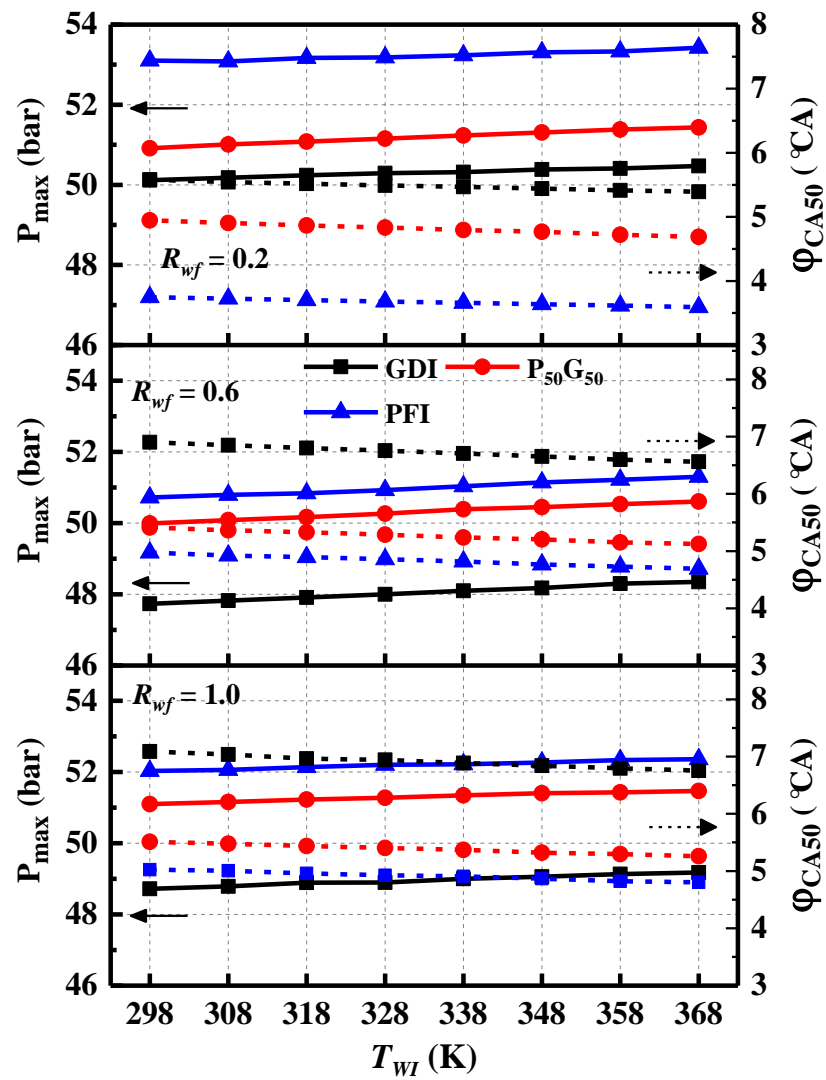
Figure 17. Effects of T_{WI} on P_{max} and φ_{CA50} (R_{wf} = 0.2, 0.6, 1.0).
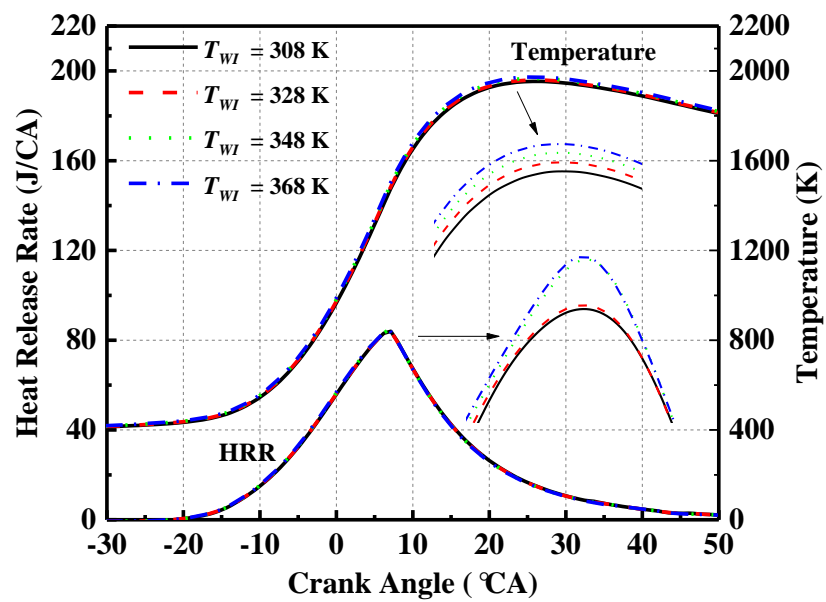
Figure 18. Effects of T_{WI} on HRR and in-cylinder temperature (GDI; R_{wf} = 1.0).

4. Conclusions

In order to eliminate CO_2 emissions from ICE for achieving carbon neutrality and mitigating global warming, the implementation of OFC technology in a dual-injection SI engine fuelled with gasoline was numerically studied. This study systematically explores the effects of WI strategies (mass, timing, temperature) on OFC characteristics in a dual-injection SI engine. The findings offer some important insights to help understand the performance and optimisation of dual-injection SI engine under OFC mode fuelled with gasoline. The main conclusions are summarised as follows.

1. Compared to CAC mode, it can be seen that the peaks of HRR under OFC are generally about 8 degrees advanced than CAC. The peaks of HRR curves decrease from around 110 J/CA of CAC to 90 J/CA of OFC. Furthermore, there is a significant increase of around 68 g/kWh in BSFC under OFC. θ_F is significantly prolonged, and the spark timing is obviously advanced. Besides, θ_C of PFI is a bit shorter than that of GDI and P_{50}-G_{50}.
2. With the increase of R_{wf}, P_{max} and in-cylinder temperature is reduced, while φ_{CA50} and the peak of HRR is postponed. There is a small benefit to BSFC under low R_{wf}. However, with the further increase of R_{wf} from 0.2 to 0.9, there is an increment of 4.29%, 3.6% and 3.77% in BSFC for GDI, P_{50}-G_{50} and PFI, respectively.
3. On the whole, the relatively lower BSFC generally appear with low R_{wf}. The lowest BSFC appears on the operating condition of 't_{WI} = -70 °CA, R_{wf} = 0.1', 't_{WI} = -70 °CA, R_{wf} = 0.2' and 't_{WI} = -70 °CA, R_{wf} = 0.2' for GDI, P_{50}-G_{50} and PFI, respectively.
4. Under the conditions of $R_{wf} \geq 0.8$, BSFC is strongly affected by t_{WI}. As t_{WI} postpones to around -30 °CA, with the improvement in combustion performance, BSFC has a sharp decrease of more than 6 g/kWh, and this decline is more evident under GDI injection strategy.
5. The variation of P_{max} and φ_{CA50} is less affected by T_{WI} compared to the effects of R_{wf} or t_{WI}. BSFC generally has a small decline with the increase of T_{WI} from 298 K to 368 K regardless of the injection strategy. P_{max} just presents an increase of around 0.5 bar, and whilst φ_{CA50} would be advanced by about 0.25 degrees.
6. It is feasible to implement appropriate WI strategies to control OFC characteristics and performance of a dual-injection SI engine, but the benefit in fuel economy is limited.
7. The findings of this study are beneficial to establish a conceptual and theoretical foundation for the implementation of OFC technology in dual-injection SI engines, as well as increasing the efficiency of this kind of engine. In future works, the engine efficiency under the OFC mode will be expected to further improve by various optimisation research, such as the effects of different kinds of fuel injection, intake charge components, variable valve actuation, etc.

Author Contributions: X.L.: Methodology, Software, Investigation, Data curation, Writing—original draft. Y.P.: Investigation. D.L.: Project administration. T.A.: Project administration. K.-J.R.: Conceptualization. A.A.: Supervision, Project administration, Funding acquisition. R.M.: Conceptualization. Z.P.: Methodology, Supervision, Writing—review & editing. All authors have read and agreed to the published version of the manuscript.

Conflicts of Interest: The authors declare no conflict of interest.

Abbreviations

BMEP	Brake Mean Effective Pressure (bar)
BSFC	Brake Specific Fuel Consumption (g/kWh)
CA	Crank Angle (degree)
CAC	Conventional Air Combustion
CCS	Carbon Capture and Storage
CO_2	Carbon Dioxide
DI	Direct Injection
ECU	Electronic Control Unit
ERDF	European Regional Development Fund
GDI	Gasoline Direct Injection
GHG	Greenhouse Gas
HRR	Heat Release Rate
ICE	Internal Combustion Engine
ICRC	Internal Combustion Rankine Cycle
KLSA	Knock Limited Spark Advance
MBT	Maximum Brake Torque
OFC	Oxy-Fuel Combustion
OMF	Oxygen Mass Fraction
PFI	Port Fuel Injection
P_{50}-G_{50}	50% Port Fuel Injection and 50% Gasoline Direct Injection
rpm	revolutions per minute
SI	Spark Ignition

References

1. Wimmer, K.; Sanz, W. Optimization and comparison of the two promising oxy-combustion cycles NET Power cycle and Graz Cycle. *Int. J. Greenh. Gas Control.* **2020**, *99*, 103055. [CrossRef]
2. Mondal, M.K.; Balsora, H.K.; Varshney, P. Progress and trends in CO_2 capture/separation technologies: A review. *Energy* **2012**, *46*, 431–441. [CrossRef]
3. Koytsoumpa, E.I.; Bergins, C.; Kakaras, E. The CO_2 economy: Review of CO_2 capture and reuse technologies. *J. Supercrit. Fluids* **2018**, *132*, 3–16. [CrossRef]
4. Anwar, M.N.; Fayyaz, A.; Sohail, N.F.; Khokhar, M.F.; Baqar, M.; Khan, W.D.; Rasool, K.; Rehan, M.; Nizami, A.S. CO_2 capture and storage: A way forward for sustainable environment. *J. Environ. Manag.* **2018**, *226*, 131–144. [CrossRef] [PubMed]
5. Zheng, G.; Peng, Z. Life Cycle Assessment (LCA) of BEV's environmental benefits for meeting the challenge of ICExit (Internal Combustion Engine Exit). *Energy Rep.* **2021**, *7*, 1203–1216. [CrossRef]
6. Huang, H.; Lei, H.; Liu, M.; Wang, T.; Li, C.; Guo, X.; Chen, Y.; Pan, M. Effect of superior mesenteric artery branch structure-based flow field on PEMFC performance. *Energy Convers. Manag.* **2020**, *226*, 113546. [CrossRef]
7. Pan, M.; Li, C.; Liao, J.; Lei, H.; Pan, C.; Meng, X.; Huang, H. Design and modeling of PEM fuel cell based on different flow fields. *Energy* **2020**, *207*, 118331. [CrossRef]
8. Yaverbaum, L. *Fluidized Bed Combustion of Coal and Waste Materials*; Noyes Data Corp.: Park Ridge, NJ, USA, 1977.
9. Kimura, N.; Omata, K.; Kiga, T.; Takano, S.; Shikisima, S. The characteristics of pulverized coal combustion in O_2/CO_2 mixtures for CO2 recovery. *Energy Convers. Manag.* **1995**, *36*, 805–808. [CrossRef]
10. Nozaki, T.; Takano, S.-I.; Kiga, T.; Omata, K.; Kimura, N. Analysis of the flame formed during oxidation of pulverized coal by an O_2 CO_2 mixture. *Energy* **1997**, *22*, 199–205. [CrossRef]
11. Chui, E.; Majeski, A.; Douglas, M.; Tan, Y.; Thambimuthu, K. Numerical investigation of oxy-coal combustion to evaluate burner and combustor design concepts. In *Greenhouse Gas Control Technologies-6th International Conference*; Gale, J., Kaya, Y., Eds.; Pergamon: Oxford, UK, 2003; pp. 87–93.
12. Stanger, R.; Wall, T.; Spörl, R.; Paneru, M.; Grathwohl, S.; Weidmann, M.; Scheffknecht, G.; McDonald, D.; Myöhänen, K.; Ritvanen, J.; et al. Oxyfuel combustion for CO_2 capture in power plants. *Int. J. Greenh. Gas Control.* **2015**, *40*, 55–125. [CrossRef]
13. Stephen, R. *An Introduction to Combustion: Concepts and Applications*; McGraw-Hill: New York, NY, USA, 1996.
14. Chen, L.; Yong, S.Z.; Ghoniem, A.F. Oxy-fuel combustion of pulverized coal: Characterization, fundamentals, stabilization and CFD modeling. *Prog. Energy Combust. Sci.* **2012**, *38*, 156–214. [CrossRef]
15. Bilger, R.W. Zero release combustion technologies and the oxygen economy. In Proceedings of the Fifth International Conference on Technologies and Combustion for a Clean Environment, Lisbon, Portugal, 12–15 July 1999.
16. Bilger, R.W.; Wu, Z. Carbon capture for automobiles using internal combustion Rankine cycle engines. *J. Eng. Gas Turbines Power* **2009**, *131*, 034502. [CrossRef]
17. Yu, X.; Wu, Z.; Fu, L.; Deng, J.; Hu, Z.; Li, L. Study of Combustion Characteristics of a Quasi Internal Combustion Rankine Cycle Engine. In *SAE Technical Paper*; SAE International: Warrendale, PA, USA, 2013. [CrossRef]

18. Fu, L.Z.; Wu, Z.J.; Yu, X.; Deng, J. Experimental study of effect of water injection on combustion stability in internal combustion Rankine cylinder engine. *Chin. Intern. Combust. Engine Eng.* **2014**, *35*, 38–45. (In Chinese)

19. Fu, L.-Z.; Wu, Z.; Li, L.; Yu, X. Effect of Water Injection Temperature on Characteristics of Combustion and Emissions for Internal Combustion Rankine Cycle Engine. In *SAE Technical Paper*; SAE International: Warrendale, PA, USA, 2014. [CrossRef]

20. Wu, Z.J.; Yu, X.; Fu, L.Z.; Deng, J.; Hu, Z.J.; Li, L.G. A high efficiency oxyfuel internal combustion engine cycle with water direct injection for waste heat recovery. *Energy* **2014**, *70*, 110–120. [CrossRef]

21. Kang, Z.; Chen, S.; Wu, Z.; Deng, J.; Hu, Z.; Li, L. Simulation Study of Water Injection Strategy in Improving Cycle Efficiency Based on a Novel Compression Ignition Oxy-Fuel Combustion Engine. *SAE Int. J. Engines* **2018**, *11*, 935–945. [CrossRef]

22. Yu, X.; Wu, Z.; Wang, C.; Deng, J.; Hu, Z.; Li, L. Study of the Combustion and Emission Characteristics of a Quasi ICRC Engine under Different Engine Loads. In *SAE Technical Paper*; SAE International: Warrendale, PA, USA, 2014. [CrossRef]

23. Wu, Z.-J.; Yu, X.; Fu, L.-Z.; Deng, J.; Li, L.-G. Experimental study of the effect of water injection on the cycle performance of an internal-combustion Rankine cycle engine. *Proc. Inst. Mech. Eng. Part D J. Automob. Eng.* **2014**, *228*, 580–588. [CrossRef]

24. Fu, L.; Wu, Z.; Yu, X.; Deng, J.; Hu, Z.; Li, L. Experimental Investigation of Combustion and Emission Characteristics for Internal Combustion Rankine Cycle Engine under Different Water Injection Laws. *Energy Procedia* **2015**, *66*, 89–92. [CrossRef]

25. Wu, J.; Kang, Z.; Zhang, Z.; Li, Z.; Deng, J.; Wu, Z. Effects of Vessel and Water Temperatures on Direct Injection in Internal Combustion Rankine Cycle Engines. *Automot. Innov.* **2018**, *1*, 331–341. [CrossRef]

26. Li, X.; Pei, Y.; Peng, Z.; Ajmal, T.; Rana, K.-J.; Aitouche, A.; Mobasheri, R. Numerical study on the effects of intake charge on oxy-fuel combustion in a dual-injection spark ignition engine at economical oxygen-fuel ratios. *Int. J. Engine Res.* **2021**. [CrossRef]

27. An, Y.; Teng, S.; Li, X.; Qin, J.; Zhao, H.; Zhan, Z.S.; Hu, T.G.; Liu, B.; Zhong, J. Study of Polycyclic Aromatic Hydrocarbons Evolution Processing in GDI Engines Using TRF-PAH Chemical Kinetic Mechanism. In *SAE Technical Paper*; SAE International: Warrendale, PA, USA, 2016. [CrossRef]

28. Wu, M.; Pei, Y.; Qin, J.; Li, X.; Zhou, J.; Zhan, Z.S.; Guo, Q.-Y.; Liu, B.; Hu, T.G. Study on Methods of Coupling Numerical Simulation of Conjugate Heat Transfer and In-Cylinder Combustion Process in GDI Engine. In *SAE Technical Paper*; SAE International: Warrendale, PA, USA, 2017. [CrossRef]

29. Li, X.; Pei, Y.-Q.; Qin, J.; Zhang, D.; Wang, K.; Xu, B. Effect of ultra-high injection pressure up to 50 MPa on macroscopic spray characteristics of a multi-hole gasoline direct injection injector fueled with ethanol. *Proc. Inst. Mech. Eng. Part D J. Automob. Eng.* **2017**, *232*, 1092–1104. [CrossRef]

30. Ma, H.; Li, Z.; Tayarani, M.; Lu, G.; Xu, H.; Yao, X. Model-based computational intelligence multi-objective optimization for gasoline direct injection engine calibration. *Proc. Inst. Mech. Eng. Part D J. Automob. Eng.* **2019**, *233*, 1391–1402. [CrossRef]

31. Raut, A.A.; Mallikarjuna, J.M. Effects of direct water injection and injector configurations on performance and emission characteristics of a gasoline direct injection engine: A computational fluid dynamics analysis. *Int. J. Engine Res.* **2020**, *21*, 1520–1540. [CrossRef]

32. Frommater, S.; Neumann, J.; Hasse, C. A phenomenological modelling framework for particle emission simulation in a direct-injection gasoline engine. *Int. J. Engine Res.* **2021**, *22*, 1166–1179. [CrossRef]

33. Wang, X.; Zhao, H. Effect of piston shape design on the scavenging performance and mixture preparation in a two-stroke boosted uniflow scavenged direct injection gasoline engine. *Int. J. Engine Res.* **2021**, *22*, 1484–1499. [CrossRef]

34. Shi, H.; Uddeen, K.; An, Y.; Pei, Y.; Johansson, B. Multiple spark plugs coupled with pressure sensors: A new approach for knock mechanism study on SI engines. *Energy* **2021**, *227*, 120382. [CrossRef]

35. Larsson, T.; Mahendar, S.; Christiansen-Erlandsson, A.; Olofsson, U. The Effect of Pure Oxygenated Biofuels on Efficiency and Emissions in a Gasoline Optimised DISI Engine. *Energies* **2021**, *14*, 3908. [CrossRef]

36. Ikoma, T.; Abe, S.; Sonoda, Y.; Suzuki, H.; Suzuki, Y.; Basaki, M. Development of V-6 3.5-liter Engine Adopting New Direct Injection System. In *SAE Technical Paper*; SAE International: Warrendale, PA, USA, 2006. [CrossRef]

37. Wu, X.; Daniel, R.; Tian, G.; Xu, H.; Huang, Z.; Richardson, D. Dual-injection: The flexible, bi-fuel concept for spark-ignition engines fuelled with various gasoline and biofuel blends. *Appl. Energy* **2011**, *88*, 2305–2314. [CrossRef]

38. Daniel, R.; Xu, H.; Wang, C.; Richardson, D.; Shuai, S. Gaseous and particulate matter emissions of biofuel blends in dual-injection compared to direct-injection and port injection. *Appl. Energy* **2013**, *105*, 252–261. [CrossRef]

39. Liu, H.; Wang, Z.; Long, Y.; Xiang, S.; Wang, J.; Fatouraie, M. Comparative study on alcohol–gasoline and gasoline–alcohol Dual-Fuel Spark Ignition (DFSI) combustion for engine particle number (PN) reduction. *Fuel* **2015**, *159*, 250–258. [CrossRef]

40. Zhuang, Y.; Zhu, G.; Gong, Z.; Wang, C. Experimental and numerical investigation of performance of an ethanol-gasoline dual-injection engine. *Energy* **2019**, *186*, 115835. [CrossRef]

41. Li, J.; Liu, C.; Kang, R.; Zhou, L.; Wei, H. Effects of the injection timing on knock and combustion characteristics in dual-fuel dual-injection engines. *Proc. Inst. Mech. Eng. Part D J. Automob. Eng.* **2020**, *234*, 2578–2591. [CrossRef]

42. Huang, Y.; Surawski, N.C.; Zhuang, Y.; Zhou, J.L.; Hong, G. Dual injection: An effective and efficient technology to use renewable fuels in spark ignition engines. *Renew. Sustain. Energy Rev.* **2021**, *143*, 110921. [CrossRef]

43. Liu, K.; Li, Y.; Yang, J.; Deng, B.; Feng, R.; Huang, Y. Comprehensive study of key operating parameters on combustion characteristics of butanol-gasoline blends in a high speed SI engine. *Appl. Energy* **2018**, *212*, 13–32. [CrossRef]

44. Teodosio, L.; Pirrello, D.; Berni, F.; De Bellis, V.; Lanzafame, R.; D'Adamo, A. Impact of intake valve strategies on fuel consumption and knock tendency of a spark ignition engine. *Appl. Energy* **2018**, *216*, 91–104. [CrossRef]

45. Tornatore, C.; Bozza, F.; De Bellis, V.; Teodosio, L.; Valentino, G.; Marchitto, L. Experimental and numerical study on the influence of cooled EGR on knock tendency, performance and emissions of a downsized spark-ignition engine. *Energy* **2019**, *172*, 968–976. [CrossRef]
46. Tian, Z.; Zhen, X.; Wang, Y.; Liu, D.; Li, X. Combustion and emission characteristics of n-butanol-gasoline blends in SI direct injection gasoline engine. *Renew. Energy* **2020**, *146*, 267–279. [CrossRef]
47. Woschni, G. A Universally Applicable Equation for the Instantaneous Heat Transfer Coefficient in the Internal Combustion Engine. In *SAE Technical Paper*; SAE International: Warrendale, PA, USA, 1967. [CrossRef]
48. Shayler, P.J.; May, S.A.; Ma, T. Heat Transfer to the Combustion Chamber Walls in Spark Ignition Engines. In *SAE Technical Paper*; SAE International: Warrendale, PA, USA, 1995.
49. Heywood, J.B. *Internal Combustion Engine Fundamentals*, 2nd ed.; McGraw-Hill: New York, NY, USA, 2018.
50. Shaddix, C.R.; Molina, A. Particle imaging of ignition and devolatilization of pulverized coal during oxy-fuel combustion. *Proc. Combust. Inst.* **2009**, *32*, 2091–2098. [CrossRef]
51. Molina, A.; Shaddix, C.R. Ignition and devolatilization of pulverized bituminous coal particles during oxygen/carbon dioxide coal combustion. *Proc. Combust. Inst.* **2007**, *31*, 1905–1912. [CrossRef]
52. Mazas, A.N.; Fiorina, B.; Lacoste, D.A.; Schuller, T. Effects of water vapor addition on the laminar burning velocity of oxygen-enriched methane flames. *Combust. Flame* **2011**, *158*, 2428–2440. [CrossRef]